

Sequential Preparation of Dual-Layer Fluorine-Doped Tin Oxide Films for Highly Efficient Perovskite Solar Cells

Kun-Mu Lee,^{*[a, b, c]} Min-Yao Hou,^[a] Vembu Suryanarayanan,^[d] and Ming-Chung Wu^{*[a, b, c]}

A dual-layer fluorine-doped tin oxide (FTO) film has been fabricated by means of sequential spray pyrolysis for high-efficiency perovskite solar cells (PSCs). The H-FTO/L-FTO dual layer film consists of a H-FTO layer prepared at high deposition temperature ($\approx 450^\circ\text{C}$) and a L-FTO layer, fabricated at low deposition temperature ($\approx 150^\circ\text{C}$), which is used to replace the traditional compact TiO_2 /FTO layer. The effects of F/Sn molar ratio, precursor solution concentration, and deposition temperature on the electrical, optical, surface morphological, and grain structural characteristics of H-FTO layers have been studied systematically. With an increase in precursor solution concentration, the mobility and carrier concentration of H-FTO increases; however, the grain size and sheet resistance decreases as the precursor solution concentration increases. A high deposition tem-

perature results in a large grain size and enhanced haze value. The L-FTO layer expresses compact layer growth, inconsistent with the H-FTO surface structure, and possesses excellent electron collection and transport efficiency. The effect of the hole-blocking characteristics of L-FTO on the PSC performance is studied. This study provides a novel dual-layer FTO film to replace the traditional compact TiO_2 /FTO layer, which is usually prepared by coating TiO_2 precursor on FTO following calcination at 450°C . The H-FTO/L-FTO dual-layer film can simplify the fabrication process and maintain a high power conversion efficiency (PCE); this results in more efficient electron transportation and blocking of holes. The champion device of PSCs with H-FTO/L-FTO shows the highest PCE of 17.37% under the illumination of 100 mW cm^{-2} (AM1.5G).

Introduction

Organic-inorganic hybrid perovskite-structured solar cell (PSC; $\text{CH}_3\text{NH}_3\text{PbI}_3$, methylammonium lead iodide (MAPbI_3)) devices have attracted much attention, owing to their increasing power conversion efficiency (PCE) from 3.8% in 2009 to the latest world record of 22.7%.^[1,2] As a result of their outstanding optoelectronic characteristics, such as high absorption coefficient,^[3] low exciton binding energy of about 0.03 eV,^[4] long carrier diffusion length,^[5] and tunable energy band gap,^[6] the PCE has been improved. With all of the advantageous properties mentioned above, perovskite-structured materials are believed to be suitable light absorbers in solar cell, laser, photo-


detector, and light-emitting devices.^[7] Various methods of perovskite film preparation have been developed. Some of these processes include a one-step solution process,^[8] the modified sequential deposition technique,^[9] the dual-source thermal evaporation technique,^[10] and a vapor-assisted solution process.^[11] Most PSCs are based on a compact layer containing mesoscopic transition-metal oxides, such as TiO_2 ,^[12] ZnO ,^[13] and SnO_2 .^[14] In addition, CdSe nanocrystals have been employed as an electron transport/extraction layer for PSCs due to high electron mobility and solution processability at low temperatures.^[15] Recently, PSCs have also been fabricated by employing a fullerene compact layer as the bottom n-type charge-extraction layer.^[16,17] Perovskite-structured materials deposited onto compact TiO_2 /mesoporous TiO_2 layers (electron transport layer (ETL)) with a high PCE have been widely studied. These studies commonly focus on how TiO_2 acts as a scaffold and how to improve perovskite coverage.^[8] The challenge of using TiO_2 is the requirement for a complicated, high-temperature ($>450^\circ\text{C}$) process. Nowadays, SnO_2 ^[14b,18] and doped SnO_2 ^[14a,19] are used as effective ETLs, on account of their high optical transmission and low-temperature fabrication processes. Yan et al. demonstrated that PSCs with SnO_2 annealed at low temperature exhibited higher photovoltaic performance than that of SnO_2 annealed at high temperature.^[18a] Liu et al. reported that PSCs with a Nb: SnO_2 film had a higher fill factor (FF) in a low-temperature process and could passivate electron traps effectively, and thus, resulted in high electron mobility.^[14a] Moreover, considering high electron mobility equally in both directions, the effectiveness of ETLs may be further increased if

[a] Prof. K.-M. Lee, M.-Y. Hou, Prof. M.-C. Wu
Department of Chemical and Materials Engineering
Chang Gung University
Taoyuan 33302 (Taiwan)
E-mail: kmlee@mail.cgu.edu.tw
mingchungwu@mail.cgu.edu.tw

[b] Prof. K.-M. Lee, Prof. M.-C. Wu
Division of Neonatology, Department of Pediatrics
Chang Gung Memorial Hospital
Linkou, Taoyuan 33305 (Taiwan)

[c] Prof. K.-M. Lee, Prof. M.-C. Wu
Center for Reliability Sciences and Technologies
Chang Gung University, Taoyuan 33302 (Taiwan)

[d] Dr. V. Suryanarayanan
Electro Organic Division
Central Electrochemical Research Institute
Karaikudi 630 006, Tamil Nadu (India)

 Supporting Information and the ORCID identification number(s) for the author(s) of this article can be found under:
<https://doi.org/10.1002/cssc.201801249>.

electron back-flow can be suppressed. Therefore, a gradient heterojunction (GHJ) strategy has been widely applied to facilitate charge separation in silicon and organic solar cells. The potential gradient creates an appropriately structured heterojunction that acts as a driving force to promote electron transport in the desired direction.^[20] Dual-layered ETLs, such as ZnO/TiO₂ and SnO₂/TiO₂, with a heterojunction potential gradient are favorable for electron extraction. Therefore, they have been widely used to improve the performance of PSCs.^[21] However, the architectures of such dual-layered ETLs are planar and often show apparent *J-V* hysteresis behavior. On the other hand, transparent conducting oxides (TCOs) have been prepared from both organic and inorganic materials for photovoltaic applications. In general, TCO layers consist of three inorganic films, including indium tin oxide (ITO), fluorine-doped tin oxide (FTO), and doped zinc oxide. Organic films with high transparency to IR light are prepared from a polymer network, for example, poly(3,4-ethylenedioxythiophene) and derivatives of poly(3,4-ethylenedioxythiophene), such as graphene and a carbon nanotube network. For efficient carrier transport, TCOs applied in optoelectronic devices, including sensors, photovoltaics, and flat panel displays, exhibit transmittance 80% greater than that of incident light and conductivities higher than 10³ S cm⁻¹. Due to defects and grain boundaries in PSCs, the transmittance of TCO films can result in light scattering. To prevent light absorption over most of the solar spectrum, a band gap greater than 3.2 eV and a carrier concentration of 10²⁰ cm⁻³ for low resistivity of the TCO thin-film electrodes are necessary. FTO not only has better stability under atmospheric conditions, better resistance to high temperature, and high tolerance to physical abrasion, but also it is chemically inert and cheaper than ITO. Hence, FTO has been considered as a potential material. FTO preparation methods include chemical vapor deposition,^[22] spray pyrolysis,^[23] and magnetron sputtering.^[24] Among these methods, spray pyrolysis stands out for many advantages. These include simple, inexpensive experimental procedures, high growth rate, ease of adding various doping materials, and the possibility of mass production for large, uniform coatings. The use of this method to fabricate doped tin oxide thin films is preferred. Moreover, to increase absorption, light scattering, and the PCE of the solar cells, textured transparent conductors have been investigated in both organic and amorphous Si solar cells.^[25] The surface roughness and light-trapping structure are correlated to the haze of the film. With a higher surface roughness, it is prone to scatter and refract light at different angles, and results in a longer light transmission path in the film. Therefore, we could efficiently assimilate the incident light. Although FTO is an important constituent of PSCs, studies on the properties of FTO that affect the performance of PSCs have not been conducted.

Herein, we demonstrate a sequential process to prepare the H-FTO/L-FTO dual layer, which consists of a high transmittance and low sheet resistance H-FTO layer prepared at high deposition temperature and a hole blocking layer of L-FTO, which is a compact layer prepared at low deposition temperature. For the H-FTO layer, we conducted studies on the effects of F/Sn molar ratio; concentration and film deposition temperature;

and electrical, morphological, and optical properties. The effect of L-FTO deposition temperature on cell performance and surface morphology of PSCs are also investigated. Moreover, the L-FTO/*meso*-TiO₂ GHJ interlayer configuration inside ETLs simultaneously achieves effective extraction and efficient transport of photoelectrons. With such an interlayer configuration, GHJs formed at the perovskite/ETL interface act collectively to extract electrons from the perovskite layer. GHJs formed at the boundaries of interconnected SnO₂ and *meso*-TiO₂ throughout the entire ETL layer, and thus, could extract electrons from the slow electron mobility of *meso*-TiO₂ to the high electron mobility of the FTO film. Therefore, the GHJ can further prevent electron back-flow and allow the use of FTO films for electron transport.

Experimental Section

Preparation of H-FTO/L-FTO dual layer

To optimize the parameters for the preparation of the H-FTO/L-FTO dual layer, a precursor solution containing SnCl₂·2H₂O (7.11 g; Aldrich) and NH₄F (1.11 g; Aldrich) in distilled water (50 mL) was prepared. The pH was maintained at 2.0 by adding HCl (Aldrich). The H-FTO/L-FTO dual layer was coated on the glass substrate by means of precursor solution spray pyrolysis in an open environment under various substrate temperatures. Dry air was used as the gas carrier during the coating process and the precursor flux was 10 L min⁻¹ continuously. Before the coating process, glass substrates were cleaned in an ultrasonic cleaner for 30 min with a solution of surfactant, rinsed in ethanol for 30 min, and dried in air. For the preparation of the H-FTO layer, the glass substrate temperatures were maintained at various temperatures, including 400 (H-FTO-400), 450 (H-FTO-450), and 500 °C (H-FTO-500). The spray time (*t_s*) was maintained at 15 min and the distance between the spray nozzle and substrate was maintained at 30.0 cm. For the L-FTO layer to form a thin compact layer, the precursor solution was sprayed on the H-FTO layer at 100 (L-FTO-100), 150 (L-FTO-150), and 200 °C (L-FTO-200) for 5 min. In comparison, the TiO₂ compact layer (reference sample) was fabricated by spray pyrolysis with the precursor solution at 450 °C.

Fabrication of PSCs

Methylammonium iodide (MAI) was composed of CH₃NH₂ (27.9 mL; 40% in methanol, Aldrich), mixed with HI (30.0 mL; 57 wt% in water, Aldrich) in a 250.0 mL round-bottomed flask, and stirred at 0 °C for 4 h. The precipitate was retrieved by evaporation at 55 °C for 1 h. MAI was then dissolved in ethanol, recrystallized from diethyl ether, and dried at 60 °C in a vacuum oven for 24 h.

By using neutral wash solution (Extran[®] MA 02, Merck Inc.), acetone, and isopropanol, the H-FTO/L-FTO and H-FTO/reference samples were cleaned. The substrate was dried at 80 °C for 24 h followed by UV-ozone treatment for 10 min. A mesoporous TiO₂ film (particle size: ≈ 20 nm, crystalline phase: anatase) with a thickness of 150 nm was screen printed onto the substrate by using home-made pastes and finally heated at 500 °C for 30 min.

After cooling to room temperature, the substrate was transferred to a glove box filled with nitrogen. A solution of PbI₂ (1.25 M) and MAI (1.25 M) in γ -butyrolactone (GBL) and DMSO (in a ratio of 5/5, v/v) was spin-coated onto the substrate through a two-step pro-

cess at 1000 rpm for 10 s followed by 5000 rpm for 20 s. The substrate was treated with toluene (100.0 μL) by drop-casting during the second spin-coating step. The substrate was then dried on a hot plate at 100 $^{\circ}\text{C}$ for 10 min. A solution of N₂,N₂,N₂',N₂',N₇,N₇,N₇',N₇'-octakis(4-methoxyphenyl)-9,9'-spiro-bi[9H-fluorene]-2,2',7,7'-tetramine (spiro-OMeTAD) was intermixed with a solution of lithium bis-trifluoromethanesulfonimide (Li-TFSI; 17.5 μL , 520 mg), acetonitrile (1.0 mL), and 4-*tert*-butylpyridine (28.5 μL). The solution was spin-coated onto the substrate at 2000 rpm for 30 s. Finally, a silver layer of 100 nm thick was deposited as the metal electrode by thermal evaporation. The device structure is shown in Figure S1 in the Supporting Information. By using a shadow mask during Ag evaporation, the active area of the solar cell of 0.16 cm^2 was defined.

Measurement of material properties

XRD patterns were measured on a Siemens Kristalloflex diffractometer (D5000, Siemens) with $\text{Cu}_{\text{K}\alpha}$ radiation ($\lambda = 1.534 \text{ \AA}$). A field-emission (FE) scanning electron microscope (Hitachi S-800) operated at 10.0 kV was employed to observe the surface microstructure. The surface morphology could be observed by tapping mode of a Digital Instruments multimode scanning probe microscope through AFM (E-sweep, SEIKO). A UV/Vis/near-infrared (NIR) spectrophotometer (U4100, HITACHI) was utilized to record the thin-film transmittance. Whole measurements were applied to determine the characteristics of the film, such as carrier mobility and carrier concentration. To measure the sheet resistance of Ag-deposited films by using the appropriate correction factors, the four-point probe was used. A surface profile meter (Tencor P15, KLA TENCOR) was used to measure the thickness of the films.

Measurements of photovoltaic characteristics

In this study, a 3A (AAA) solar simulator (KXL-500F, Wacom, Japan) was used. The solar simulator was composed of a NREL-certified silicon solar cell (Oriol, 91150 V), with a KG-5 bandpass filter, and the light intensity was fixed at 100 mW cm^{-2} (AM1.5G). By using a computer-controlled digital source meter (2400, Keithley), J - V curves of photovoltaic devices could be estimated, and the photovoltaic devices were measured from forward bias to short circuit (FB-SC; reverse scanning) and in reverse (SC-FB; forward scanning). The modified J - V hysteresis index^[26] was defined by using Equation (1):

$$\text{hysteresis index} = \frac{J_{\text{RS}} - J_{\text{FS}}}{J_{\text{RS}}} \quad (1)$$

in which J_{FS} and J_{RS} are the current densities of the forward and reverse scans, respectively, which were measured at 80% open-circuit voltage (V_{oc}). The incident photon-to-electron conversion efficiency (IPCE) spectra were measured in a black box by using a commercial IPCE measurement system (QE-R, Enlitech).

Results and Discussion

Effect of F/Sn ratio and precursor concentration on the H-FTO layer

Uniform, high-quality, dual-layer L-FTO/H-FTO films were prepared with optimal optical and electrical properties at controlled deposition temperatures by means of the spray pyrolysis method. The H-FTO layer composition has a significant

impact on determining high conductivity with high utilization of light in PSCs. For the FTO-coated glass slide, fluorine atoms act as shallow-level n-type dopants to create more free electrons in the samples, which can lead to high conductivity. The physical properties of various H-FTO layers fabricated with different F/Sn molar ratios are shown in Figure 1. With increasing molar ratio of F/Sn, the carrier concentration and mobility increase. At a F/Sn molar ratio of 0.8, the mobility reaches a maximum of about $28.2 \text{ cm}^2 \text{ V}^{-1}$ (Figure 1a). The transmittance initially decreases with increasing fluorine concentration, and it is not until the molar ratio of F/Sn reaches 0.5 that the transmittance increases with further increases in fluorine concentration (Figure 1b). Reflectance decreases in the visible region, but is enhanced in the NIR region with increasing fluorine concentration. The result above indicates that, during the doping process, only a few fluorine atoms could fill the oxygen vacancies, which would result in a lower concentration of scattering centers and increasing mobility of the F-doped films (Figure 1c). However, once it exceeds the limit of incorporated F content, the electron mobility would be reduced and the resistance of the H-FTO layer (with smaller grain size) would be increased.^[23c,27] Figure 1d shows the XRD patterns of predominant changes to the (110) and (211) planes with increasing molar ratio of F/Sn. Furthermore, in the XRD patterns, the signal of the (200) plane disappeared and the signal of the (301) plane appeared. However, with increasing concentration of fluorine ions, the preferred orientation changes from (110) to (211) planes. The growth changes can be analyzed based on structure factor calculations.^[28] The results imply that tin atoms occupy only regular lattice sites at a low molar ratio of F/Sn. However, if the concentration of fluorine ions exceeds the limit, tin occupation of interstitial sites gradually occurs, which results in preferred growth changes to the film.^[29]

Similar results are also obtained for the effect of the F/Sn ratio upon increasing the concentration of SnCl_2 , while keeping the F/Sn molar ratio at 0.8. As shown in Figure 2a, XRD patterns show predominant changes to the (110) and (211) planes upon increasing the concentration of SnCl_2 . Figure 2b reports the lowest sheet resistance of $(6.3 \pm 0.1) \Omega \square^{-1}$ at 1.0 M SnCl_2 . The resistance increases at higher concentrations and the transmittance decreases. The reflectance decreases in the visible region, but increases in the NIR region with increasing precursor concentration because of the increase in film thickness and density of scattering centers in the H-FTO layer. Because the decomposition temperature of ammonium fluoride is quite low ($< 100 \text{ }^{\circ}\text{C}$), the instantaneous formation of a cloud of HF in the vicinity of the growing SnO_2 film may result in etching of the film. The competitive evolution of HF [Eqs. (2) and (3)] may determine the rate of deposition of the SnO_2 film.^[30]



Equations (1) and (2) show that fluorine evolution leads to a delay in the formation of the FTO layer. Hence, 1.0 M SnCl_2 and a F/Sn molar ratio of 0.8 was preferred in our studies.

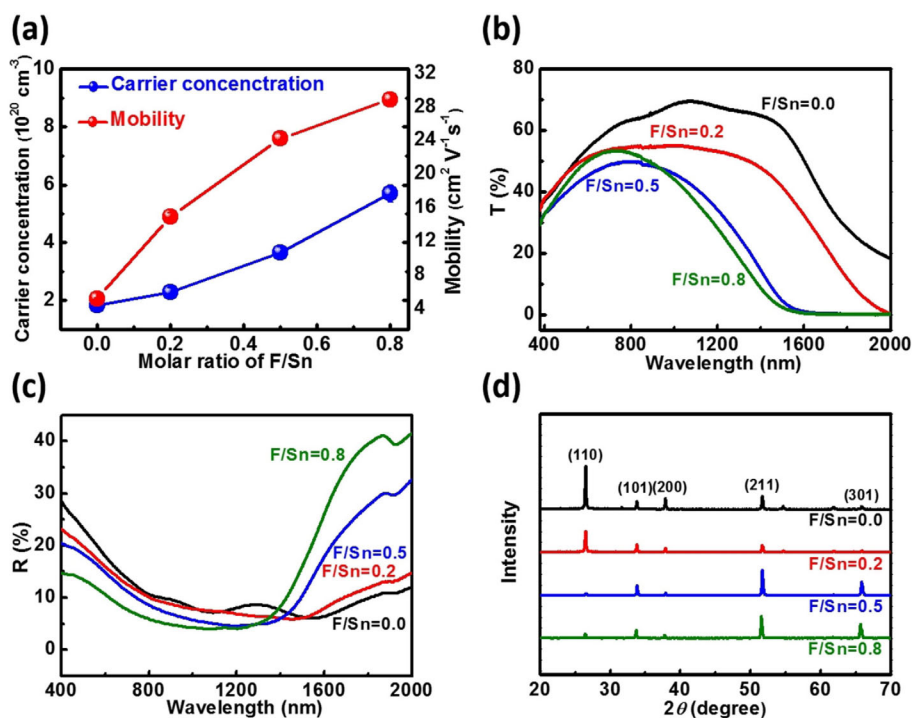


Figure 1. a) Plot of carrier concentration and mobility, b) transmittance spectra, c) reflectance spectra, and d) XRD patterns of H-FTO layers with various F/Sn molar ratios.

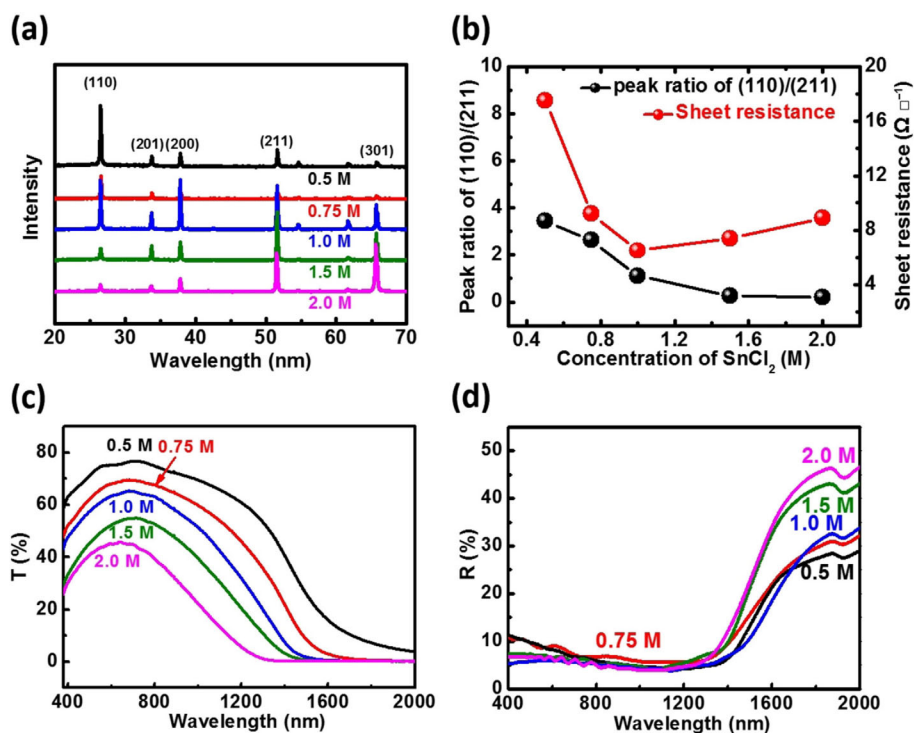


Figure 2. a) XRD patterns, b) a plot of peak ratios of (110)/(211) and film sheet resistance, c) transmittance spectra, and d) reflectance spectra of H-FTO layers with various concentrations of SnCl_2 , with a constant F/Sn molar ratio of 0.8.

Effect of deposition temperatures on H-FTO and L-FTO layers

Figure 3 shows surface microstructure, cross-section, and AFM topographic images of the H-FTO layer deposited at 400, 450, and 500 °C. The morphology evidently changes with temperature. The grain size and thickness of the H-FTO layer increase as the deposition temperature increases. More scattering centers result in a lower free electron diffusion rate (higher sheet resistance of film) if the H-FTO layer is deposited at lower temperatures. As the deposition temperature increases, the grain size of the H-FTO layer significantly increases, and the carrier mobility increases as the grain boundary decreases. The free electron diffusion rate is enhanced, leading to a low sheet resistance.

The XRD patterns of H-FTO layers prepared on a glass substrate at 400, 450, and 500 °C are shown in Figure S2 in the Supporting Information. An apparent overview of relative changes in peak intensities corresponding to different crystal orientations is given. The peak positions of the H-FTO layer are homologous with the patterns of a tetragonal crystal structure.

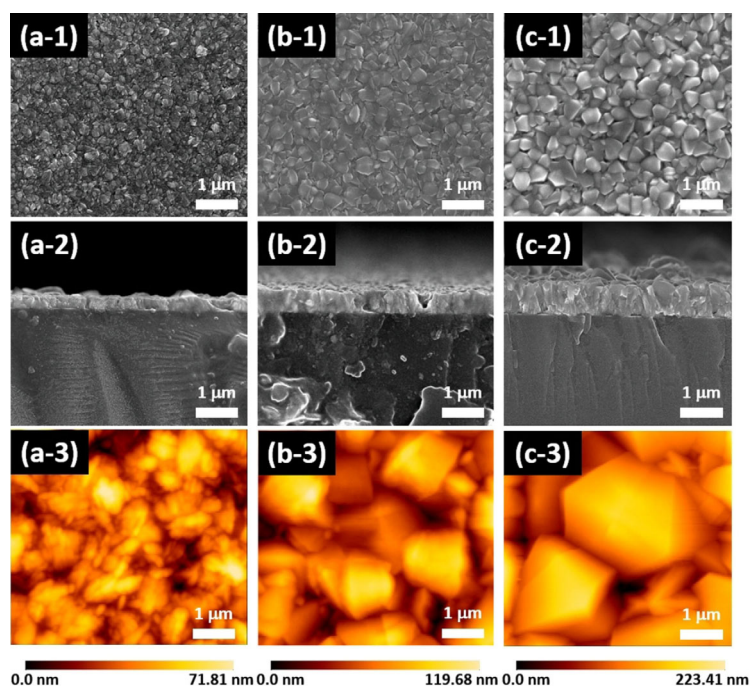


Figure 3. Surface microstructure (1), cross-section (2), and AFM topographic (3) images of various H-FTO layers deposited at 400 (a), 450 (b), and 500 °C (c).

As the temperature of the substrate increases, the intensity of all planes increases. Suitable growth undoubtedly prefers a high deposition temperature and specific interactions between the nucleus and surface. The applicable orientation of the crystal plane is related to the interaction of surface energy and the orientation of the plane; a low surface energy interaction is favorable.^[31] Other properties of H-FTO layers are listed in Table 1. As the deposition temperature increases, the grain sizes and RMS roughness of various H-FTO layers increase from 34.6 to 46.5 nm and from 15.2 to 37.0 nm, respectively. The phenomenon mentioned above leads to a transmittance decrease and an increase in haze from around 10 to 35% (Figure 4). Herein, with increasing deposition temperature (400 to 500 °C), the sheet resistance decreases (14.2 to 7.9 Ω/□). The haze value represents the film surface topography behavior and light-trapping level. Although an increase in deposition temperature leads to an increase in haze value, the high degree of surface roughness distributes the light at several angles through refraction and scattering. This induced longer light-passing length exists in perovskite films that are several hundreds of nanometers thick and efficiently assimilates incident light. Hence, we chose the more advantageous H-FTO-450 layer for further study.

After obtaining the H-FTO-450 layer, the L-FTO compact layer was sequentially deposited with precursor at 100, 150, and 200 °C, as a hole blocking layer for PSCs. Figure 5 shows the surface microstructure, cross-section, and AFM topographic images of reference sample and various L-FTO compact layers spray coated on the H-FTO-450 layer. The reference sample shown in Figure 5a used for comparison was a compact layer of about 50 nm thick TiO₂ coated on the H-FTO layer, which was calcined at 500 °C. L-FTO-100 does not form a continuous film, and thus, leads to the appearance of several block L-FTO (Figure 5b). Due to the slow reaction rate of the sprayed precursor, clusters partially react to form sediment, leading to many areas of H-FTO remaining uncovered by L-FTO. Therefore, the film is not compact and is not able to obstruct holes effectively, and thus, leads to severe shunting paths and interface electron/hole recombination. The SEM image of L-FTO-150 expresses compact layer growth along the H-FTO-450 surface (≈ 50 nm; Figure 5c). If the temperature reaches 200 °C, large protrusion deposits are formed with thicker L-FTO layers (≈ 75 nm; Figure 5d). The in-

Table 1. Electrical properties of H-FTO films fabricated at various temperatures.^[a]

H-FTO	T_s [°C]	RMS roughness [nm]	Grain size [nm]	Resistivity [Ω cm]	R_s [Ω/□]	Carrier conc. [10 ²⁰ cm ⁻³]	Mobility [cm ² V ⁻¹ s ⁻¹]
H-FTO-400	400	15.2 ± 0.1	34.6	2.6 × 10 ⁻³	14.2 ± 0.7	9.23	1.55
H-FTO-450	450	26.7 ± 0.1	41.8	8.6 × 10 ⁻⁴	8.2 ± 0.6	6.66	18.34
H-FTO-500	500	37.0 ± 0.1	46.5	5.9 × 10 ⁻⁴	7.9 ± 0.6	5.38	21.47

[a] The molar ratio of F/Sn is 0.8 and the deposition time is 10 min. T_s = substrate temperature; RMS (root-mean-square) roughness and grain size are measured and calculated from AFM and XRD analyses, respectively; R_s = sheet resistance.

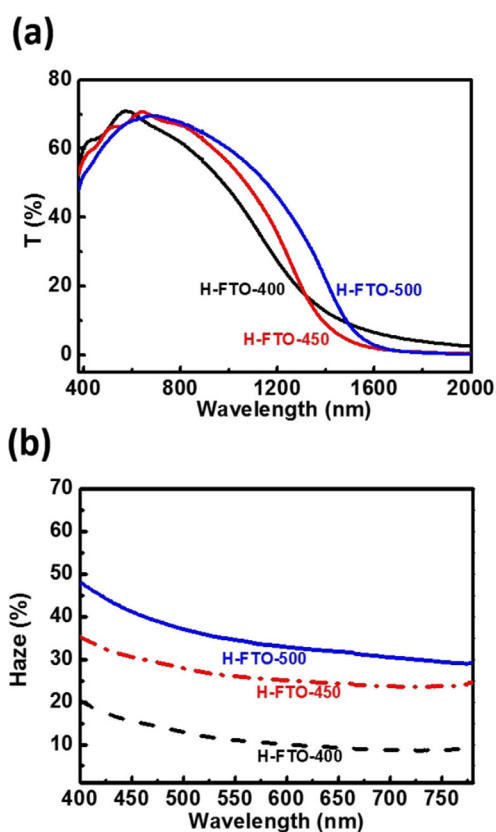


Figure 4. a) Transmittance and b) haze spectra of various H-FTO layers deposited at 400, 450, and 500 °C.

creasing L-FTO thickness at higher temperature is due to the high reaction rate of L-FTO, upon which the precursor is actively deposited once brought into contact with the substrate by the carrier gas. AFM images confirm that the L-FTO-200 film is rougher than that of the L-FTO-150 film. The RMS roughnesses of L-FTO-150 and L-FTO-200 films deposited on H-FTO-450 substrates are (31.4 ± 0.1) and (34.0 ± 0.1) nm, respectively (Table 2). The UV/Vis absorbance spectra of perovskite films with various L-FTO films are shown in Figure S3 in the Supporting Information. The onset adsorption of perovskite films with various compact layers starts at $\lambda \approx 780$ nm, as confirmed by the IPCE spectra. These UV/Vis spectra are almost identical, indicating similar morphologies, due to the excellent quality of deposition on large-area, uniform, perovskite films. This reveals that perovskite film formation is not influenced by different L-FTO films. The large difference in V_{OC} and FF could be primarily due to the properties of the L-FTO layer annealed at different temperatures.

To study the mechanism of electron–hole motions, samples of perovskite film, Perovskite/L-FTO-100, Perovskite/L-FTO-150, Perovskite/L-FTO-200, and Perovskite/TiO₂ compact layer (for comparison), were prepared on H-FTO-450/glass to obtain the photoluminescence (PL) value. By performing PL measurements, we can evaluate whether the L-FTO film efficiently extracts photogenerated electrons from the perovskite film. The steady-state PL spectra of various samples are shown in Figure 6. The Perovskite/L-FTO-150 film shows respectably high PL quenching compared with those of the others. The results prove that L-FTO-150 has better electron collection and transport efficiency, which may be due to improved electron mobility.

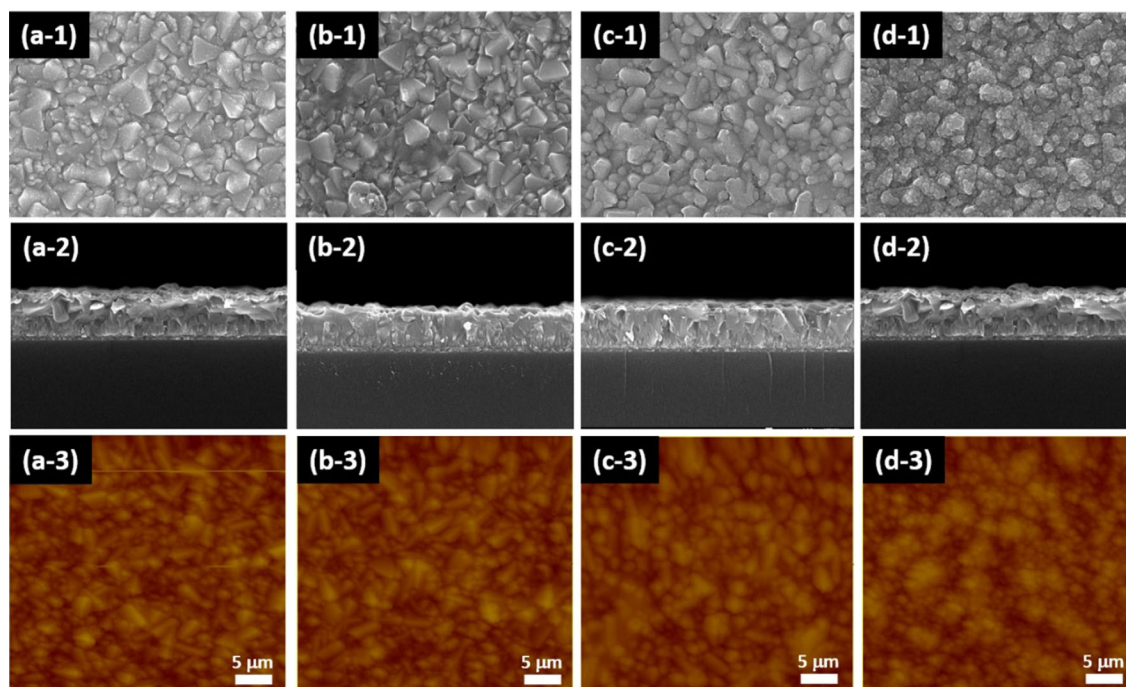


Figure 5. Surface microstructure (1), cross-section (2), and AFM topographic (3) images of reference sample (a) and the H-FTO-450 layer (deposited at 450 °C) coated with L-FTO layers deposited at 100 (b), 150 (c), and 200 °C (d).

Table 2. Film roughness of various L-FTO compact layers and the photovoltaic characteristics of PSCs under illumination of 100 mWcm⁻² (AM1.5G).

L-FTO	T _s [°C]	Roughness [nm]	Scanning direction	J _{sc} [mA cm ⁻²]	V _{oc} [V]	FF [%]	PCE [%]	Hysteresis index
Reference PSC	–	30.5 ± 0.1	reverse forward	22.02 22.03	1.057 1.049	70.7 55.4	16.46 12.80	0.209
L-FTO-100	100	32.2 ± 0.1	reverse forward	21.85 21.33	0.893 0.873	52.3 49.9	10.20 9.29	0.280
L-FTO-150	150	31.4 ± 0.1	reverse forward	22.29 22.28	1.018 1.022	76.0 67.0	17.37 15.30	0.111
L-FTO-200	200	34.0 ± 0.1	reverse forward	22.52 22.90	1.021 1.011	75.0 66.7	17.24 15.44	0.098

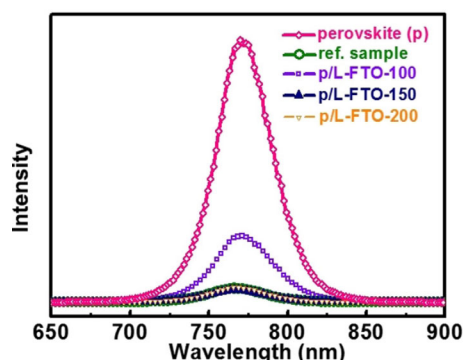


Figure 6. PL spectra of individual perovskite-structured active layers, which were coated on different substrates, including a reference sample (compact TiO₂/H-FTO-450) and various L-FTO/H-FTO-450 films.

Effect of L-FTO on PSC performance

The architectures of reference PSC and PSCs with various dual-layer L-FTO/H-FTO films are shown in Figure 7a. A cross-sectional SEM image of a PSC with the dual-layer L-FTO-150/H-FTO-450 film is shown in Figure 7b. The interface of the H-FTO and L-FTO layers has no apparent boundaries, and the thicknesses of the L-FTO/H-FTO dual layer, MAPbI₃/meso-TiO₂, HTM, and Ag layer are approximately 600, 400, 300, and 100 nm, respectively. PSCs with various L-FTO films show similar responses in the IPCE spectra (Figure 7c). In addition, the cell performance with different thicknesses of 150-L-FTO layer is obtained to understand the correlation between 150-L-FTO thickness and PCE. Various film thicknesses of the L-FTO-150 layer are demonstrated by repeating the spray cycle, and the actual thickness of the 150-L-FTO layer with various spray cycles was

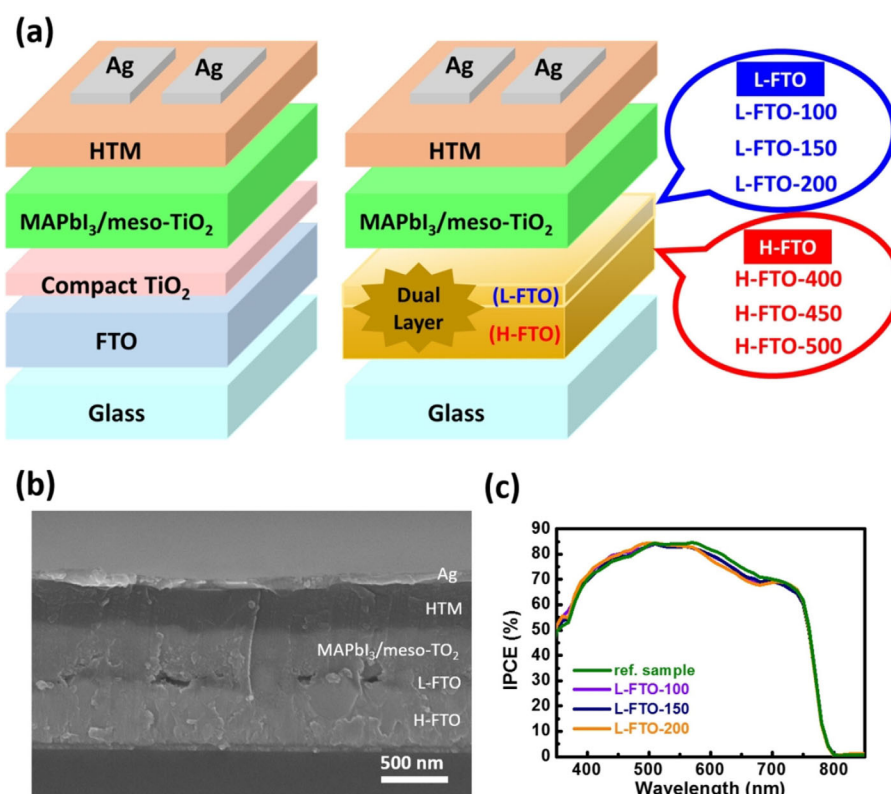


Figure 7. a) Device structure of reference PSC and PSCs with various dual-layer L-FTO/H-FTO films. HTM = hole-transporting material. b) Cross-sectional SEM image of a PSC with the dual-layer L-FTO-150/H-FTO-450 film. c) IPCE spectra of reference PSC and PSCs with various dual-layer L-FTO/H-FTO films.

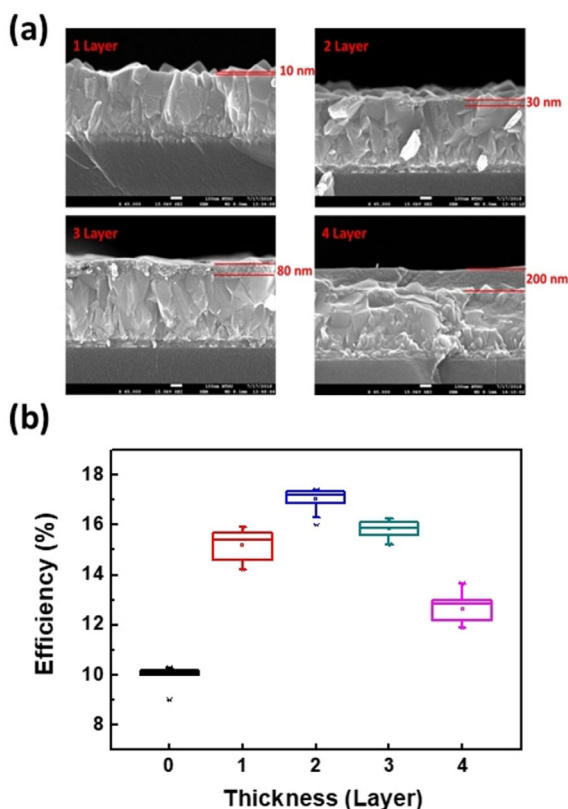


Figure 8. a) The thickness of the 150-L-FTO layer with various spray cycles of the 150-L-FTO layer. b) The cell performance distribution of PSCs (20 cells) for different thicknesses of 150-L-FTO layer.

observed by SEM (Figure 8a). The PCE distribution of 20 PSCs with different thicknesses of 150-L-FTO layer is shown in Figure 8b. The PSC with a 30 nm L-FTO-150 layer (prepared by 2 cycles) shows a high PCE of 17.4%, whereas the absence of such a layer leads to very poor light harvesting. Further increasing the number of spray cycles of the layer, the efficiency of the PSC decreases due to the increase in series resistance, as a result of enhanced thickness.

Figure 9a–c presents the J - V curves of PSCs with various L-FTO layers under illumination of 100 mW cm^{-2} (AM1.5G), and the photovoltaic characteristics of the PSCs are listed in Table 2. The PSC with L-FTO-100 shows a poor V_{OC} and FF, and those with L-FTO-150 and L-FTO-200 present higher V_{OC} , FF, and PCE values, and show similar J - V behavior. Therefore, there is no need for a higher temperature calcination process (200°C). These performances are comparable to that with the reference sample. Furthermore, we also confirmed the effect of the *meso*- TiO_2 layer in this study. The L-FTO-150 layer was only prepared for PSC, for which it showed poor cell performance with high hysteresis behavior (Figure S4 in the Supporting Information). This indicates that the *meso*- TiO_2 layer plays important roles in ETL/perovskite interface connection, electron collection, and preparation of a smooth perovskite layer. Resulting

from the intrinsically slow electron mobility of *meso*- TiO_2 film, electron back transfer and charge recombination between L-FTO/*meso*- TiO_2 and $\text{CH}_3\text{NH}_3\text{PbI}_3$ layers can be suppressed. Because direct contact between ETL and HTL can be avoided, upon preparing a compact and smooth $\text{CH}_3\text{NH}_3\text{PbI}_3$ perovskite layer, charge recombination can be decreased.^[18a] Figure 9d and e illustrates the steady-state current and conversion efficiency (J - t and η - t curve) applied with a constant bias voltage, with the architecture of glass/H-FTO/150-L-FTO/*meso*- TiO_2 / $\text{CH}_3\text{NH}_3\text{PbI}_3$ /spiro-OMeTAD/Ag, under AM1.5G illumination. The steady-state current was measured and the on/off shadow cover test process was continued for 300 s. The steady-state conversion efficiency obtained from the η - t curve was 16.77%, which approached an average efficiency of 16.33% measured from the forward and reverse scanning J - V curves.

Conclusions

High-quality, dual-layer L-FTO/H-FTO films were prepared by means of sequential spray pyrolysis deposition with controlled step temperatures. The effects of molar ratio of F/Sn, concentration of the precursor, and deposition temperature on H-FTO were investigated. With increasing precursor concentration, the carrier concentration and mobility of H-FTO increased, but the sheet resistance and grain size of H-FTO decreased. A high deposition temperature resulted in large grain size and enhanced haze value. Increasing the molar ratio of F/Sn led to changes to both the (110) and (211) planes and structural morphology. Finally, upon comparing the performance of PSCs

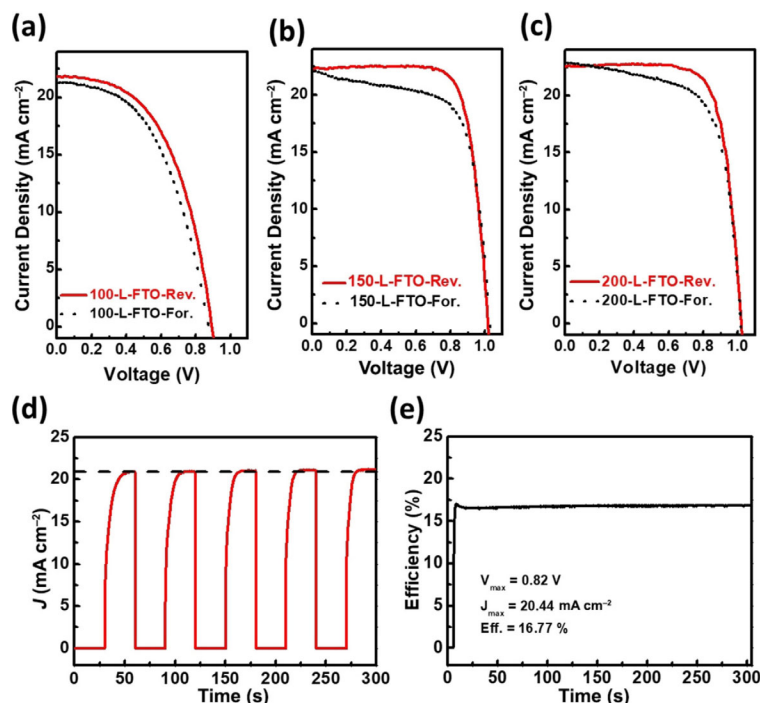


Figure 9. The J - V curves for forward and reverse scans under illumination of AM1.5G of PSCs with various L-FTO layers: a) L-FTO-100, b) L-FTO-150, and c) L-FTO-200 coated on H-FTO-450. d) J - t curve and e) η - t curve of the PSC with the dual-layer L-FTO-150/H-FTO-450 film.

with various L-FTO layers, the PSC with L-FTO-150 expressed a compact layer growth consistent with the H-FTO surface structure and had excellent electron collection. Its transport efficiency showed the highest PCE of 17.37%, with a low hysteresis index of 0.111, under the illumination of AM1.5G (100 mW cm⁻²).

Acknowledgements

We acknowledge financial support from the Ministry of Science and Technology, Taiwan (grant nos. MOST 106-2218-E-182-005-MY2 and MOST 106-2221-E-182-057-MY3), and Chang Gung Memorial Hospital, Linkou, Taiwan (CMRPD2G0301 and BMRPC074).

Conflict of interest

The authors declare no conflict of interest.

Keywords: doping · electrochemistry · fluorine · perovskite phases · solar cells

- [1] A. Kojima, K. Teshima, Y. Shirai, T. Miyasaka, *J. Am. Chem. Soc.* **2009**, *131*, 6050–6051.
- [2] a) S. I. Seok, M. Grätzel, N. G. Park, *Small* **2018**, *14*, 1704177; b) S. F. Völker, S. Collavini, J. L. Delgado, *ChemSusChem* **2015**, *8*, 3012–3028.
- [3] M. A. Green, A. Ho-Baillie, H. J. Snaith, *Nat. Photonics* **2014**, *8*, 506–514.
- [4] A. Miyata, A. Mitoglu, P. Plochocka, O. Portugall, J. T.-W. Wang, S. D. Stranks, H. J. Snaith, R. J. Nicholas, *Nat. Phys.* **2015**, *11*, 582–587.
- [5] S. D. Stranks, G. E. Eperon, G. Grancini, C. Menelaou, M. J. P. Alcocer, T. Leijtens, L. M. Herz, A. Petrozza, H. J. Snaith, *Science* **2013**, *342*, 341–344.
- [6] G. E. Eperon, S. D. Stranks, C. Menelaou, M. B. Johnston, L. M. Herz, H. J. Snaith, *Energy Environ. Sci.* **2014**, *7*, 982–988.
- [7] S. D. Stranks, H. J. Snaith, *Nat. Nanotechnol.* **2015**, *10*, 391–402.
- [8] M. M. Lee, J. Teuscher, T. Miyasaka, T. N. Murakami, H. J. Snaith, *Science* **2012**, *338*, 643–647.
- [9] L. Hu, J. Peng, W. Wang, Z. Xia, J. Yuan, J. Lu, X. Huang, W. Ma, H. Song, W. Chen, Y.-B. Cheng, J. Tang, *ACS Photonics* **2014**, *1*, 547–553.
- [10] M. Liu, M. B. Johnston, H. J. Snaith, *Nature* **2013**, *501*, 395–398.
- [11] L. Hu, J. Peng, W. Wang, Z. Xia, J. Yuan, J. Lu, X. Huang, W. Ma, H. Song, W. Chen, Y.-B. Cheng, J. Tang, *ACS Photonics* **2014**, *1*, 547–553.
- [12] a) W. Ke, G. Fang, J. Wang, P. Qin, H. Tao, H. Lei, Q. Liu, X. Dai, X. Zhao, *ACS Appl. Mater. Interfaces* **2014**, *6*, 15959–15965; b) T. Ye, J. Xing, M. Petrović, S. Chen, V. Chellappan, G. S. Subramanian, T. C. Sum, B. Liu, Q. Xiong, S. Ramakrishna, *Sol. Energy Mater. Sol. Cells* **2017**, *163*, 242–249.
- [13] a) X. Zhao, H. Shen, Y. Zhang, X. Li, X. Zhao, M. Tai, J. Li, J. Li, H. Lin, *ACS Appl. Mater. Interfaces* **2016**, *8*, 7826–7833; b) Y. Dkhissi, S. Meyer, D. Chen, H. C. Weerasinghe, L. Spiccia, Y.-B. Cheng, R. A. Caruso, *ChemSusChem* **2016**, *9*, 687–695.
- [14] a) X. Ren, D. Yang, Z. Yang, J. Feng, X. Zhu, J. Niu, Y. Liu, W. Zhao, S. F. Liu, *ACS Appl. Mater. Interfaces* **2017**, *9*, 2421–2429; b) Y. Lee, S. Lee, G. Seo, S. Paek, K. Cho, A. Huckaba, M. Calizzi, D.-W. Choi, J.-S. Park, D. Lee, H. Joong Lee, A. M. Asiri, M. Nazeeruddin, *Adv. Sci.* **2018**, *5*, 1800130.
- [15] a) X. Zeng, T. Zhou, C. Leng, Z. Zang, M. Wang, W. Hu, X. Tang, S. Lu, L. Fang, M. Zhou, *J. Mater. Chem. A* **2017**, *5*, 17499–17505; b) F. Tan, W. Xu, X. Hu, P. Yu, W. Zhang, *Nanoscale Res. Lett.* **2017**, *12*, 614.
- [16] S. Collavini, I. Kosta, S. F. Völker, G. Cabanero, H. J. Grande, R. Tena-Zaera, J. L. Delgado, *ChemSusChem* **2016**, *9*, 1263–1270.
- [17] K. Wojciechowski, T. Leijtens, S. Siprova, C. Schlueter, M. T. Hörantrner, J. T.-W. Wang, C.-Z. Li, A. K. Y. Jen, T.-L. Lee, H. J. Snaith, *J. Phys. Chem. Lett.* **2015**, *6*, 2399–2405.
- [18] a) W. Ke, D. Zhao, A. J. Cimaroli, C. R. Grice, P. Qin, Q. Liu, L. Xiong, Y. Yan, G. Fang, *J. Mater. Chem. A* **2015**, *3*, 24163–24168; b) W. Ke, G. Fang, Q. Liu, L. Xiong, P. Qin, H. Tao, J. Wang, H. Lei, B. Li, J. Wan, G. Yang, Y. Yan, *J. Am. Chem. Soc.* **2015**, *137*, 6730–6733; c) Q. Liu, M.-C. Qin, W.-J. Ke, X.-L. Zheng, Z. Chen, P.-L. Qin, L.-B. Xiong, H.-W. Lei, J.-W. Wan, J. Wen, G. Yang, J.-J. Ma, Z.-Y. Zhang, G.-J. Fang, *Adv. Funct. Mater.* **2016**, *26*, 6069–6075; d) T. Singh, J. Singh, T. Miyasaka, *ChemSusChem* **2016**, *9*, 2559–2566; e) T. Bu, S. Shi, J. Li, Y. Liu, J. Shi, L. Chen, X. Liu, J. Qiu, Z. Ku, Y. Peng, J. Zhong, Y.-B. Cheng, F. Huang, *ACS Appl. Mater. Interfaces* **2018**, *10*, 14922–14929.
- [19] a) J. Ma, G. Yang, M. Qin, X. Zheng, H. Lei, C. Chen, Z. Chen, Y. Guo, H. Han, X. Zhao, G. Fang, *Adv. Sci.* **2017**, *4*, 1700031; b) G. Yang, H. Lei, H. Tao, X. Zheng, J. Ma, Q. Liu, W. Ke, Z. Chen, L. Xiong, P. Qin, Z. Chen, M. Qin, X. Lu, Y. Yan, G. Fang, *Small* **2017**, *13*, 1601769.
- [20] a) Z. Xiao, Y. Yuan, B. Yang, J. VanDerslice, J. Chen, O. Dyck, G. Duscher, J. Huang, *Adv. Mater.* **2014**, *26*, 3068–3075; b) M. Campoy-Quiles, T. Ferrer, T. Agostinelli, P. G. Etchegoin, Y. Kim, T. D. Anthopoulos, P. N. Stavrinou, D. D. C. Bradley, J. Nelson, *Nat. Mater.* **2008**, *7*, 158; c) Y. Hou, X. Chen, S. Yang, C. Li, H. Zhao, H. G. Yang, *Adv. Funct. Mater.* **2017**, *27*, 1700878.
- [21] a) H.-S. Rao, B.-X. Chen, W.-G. Li, Y.-F. Xu, H.-Y. Chen, D.-B. Kuang, C.-Y. Su, *Adv. Funct. Mater.* **2015**, *25*, 7200–7207; b) K. Mahmood, B. S. Swain, A. Amassian, *Nanoscale* **2015**, *7*, 12812–12819.
- [22] a) J. Yang, H. Zhao, Q. Chen, S. Liu, H. Sha, F. Zhang, *Thin Solid Films* **2012**, *520*, 5691–5694; b) N. Noor, I. P. Parkin, *Thin Solid Films* **2013**, *532*, 26–30.
- [23] a) S. I. Noh, H.-J. Ahn, D.-H. Riu, *Ceram. Int.* **2012**, *38*, 3735–3739; b) H. Bisht, H. T. Eun, A. Mehrtens, M. A. Aegerter, *Thin Solid Films* **1999**, *351*, 109–114; c) A. I. Martinez, D. R. Acosta, *Thin Solid Films* **2005**, *483*, 107–113; d) P. S. Shewale, K. Ung Sim, Y.-b. Kim, J. H. Kim, A. V. Moholkar, M. D. Uplane, *J. Lumin.* **2013**, *139*, 113–118; e) M. A. Aouaj, R. Diaz, A. Belayachi, F. Rueda, M. Abd-Lefdil, *Mater. Res. Bull.* **2009**, *44*, 1458–1461; f) C. Luangchaisri, S. Dumrongrattana, P. Rakkwamsuk, *Procedia Eng.* **2012**, *32*, 663–669; g) A. V. Moholkar, S. M. Pawar, K. Y. Rajpure, S. N. Almari, P. S. Patil, C. H. Bhosale, *Sol. Energy Mater. Sol. Cells* **2008**, *92*, 1439–1444; h) C.-C. Lin, M.-C. Chiang, Y.-W. Chen, *Thin Solid Films* **2009**, *518*, 1241–1244.
- [24] a) M. Bender, W. Seelig, C. Daube, H. Frankenberger, B. Ocker, J. Stollenwerk, *Thin Solid Films* **1998**, *326*, 72–77; b) T. Jäger, B. Bissig, M. Döbeli, A. N. Tiwari, Y. E. Romanyuk, *Thin Solid Films* **2014**, *553*, 21–25.
- [25] a) F. I. Chowdhury, T. Blaine, A. B. Gougam, *Energy Procedia* **2013**, *42*, 660–669; b) C.-H. Tsai, S.-Y. Hsu, T.-W. Huang, Y.-T. Tsai, Y.-F. Chen, Y. H. Jhang, L. Hsieh, C.-C. Wu, Y.-S. Chen, C.-W. Chen, C.-C. Li, *Org. Electron.* **2011**, *12*, 2003–2011; c) Q. Huang, Y. Liu, S. Yang, Y. Zhao, X. Zhang, *Sol. Energy Mater. Sol. Cells* **2012**, *103*, 134–139; d) C.-Y. Kim, D.-H. Riu, *Thin Solid Films* **2011**, *519*, 3081–3085; e) P. I. Rovira, A. S. Ferlauto, J. Koh, C. R. Wronski, R. W. Collins, *J. Non-Cryst. Solids* **2000**, *266–269*, 279–283; f) J. Müller, B. Rech, J. Springer, M. Vanecek, *Sol Energy* **2004**, *77*, 917–930; g) Y. Nasuno, N. Kohama, K. Nishimura, T. Hayakawa, H. Taniguchi, M. Shimizu, *Appl. Phys. Lett.* **2006**, *88*, 071909.
- [26] H.-S. Kim, N.-G. Park, *J. Phys. Chem. Lett.* **2014**, *5*, 2927–2934.
- [27] A. V. Moholkar, S. M. Pawar, K. Y. Rajpure, C. H. Bhosale, J. H. Kim, *Appl. Surf. Sci.* **2009**, *255*, 9358–9364.
- [28] C. Agashe, M. G. Takwale, V. G. Bhide, S. Mahamuni, S. K. Kulkarni, *J. Appl. Phys.* **1991**, *70*, 7382–7386.
- [29] K.-M. Lee, K.-L. Shih, C.-H. Chiang, V. Suryanarayanan, C.-G. Wu, *Thin Solid Films* **2014**, *570*, 7–15.
- [30] C. Agashe, S. S. Major, *J. Mater. Sci.* **1996**, *31*, 2965–2969.
- [31] G. Gordillo, L. C. Moreno, W. de la Cruz, P. Teheran, *Thin Solid Films* **1994**, *252*, 61–66.

Manuscript received: June 4, 2018

Revised manuscript received: July 17, 2018

Accepted manuscript online: July 18, 2018

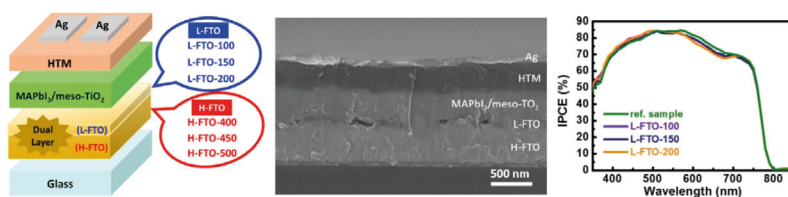
Version of record online: ■■■■■ 0000

FULL PAPERS

K.-M. Lee,* M.-Y. Hou, V. Suryanarayanan,
M.-C. Wu*



Sequential Preparation of Dual-Layer Fluorine-Doped Tin Oxide Films for Highly Efficient Perovskite Solar Cells



Turn up the heat on doping: A dual-layer, fluorine-doped tin oxide (FTO) film is fabricated through sequential spray pyrolysis for the preparation of high-efficiency perovskite solar cells. FTO layers

are prepared at high (H) and low (L) deposition temperatures to yield the H-FTO/L-FTO dual-layer film as a replacement for the traditional compact TiO₂/FTO layer.